

# X-ray Absorption Fine Structure Study of the Effect of Protonation on Disorder and Multiple Scattering in Phosphate Solutions and Solids

Ashaki A. Rouff,\* Stefan Rabe, Maarten Nachtegaal, and Frédéric Vogel

General Energy Research (ENE), Laboratory for Energy and Materials Cycles, Paul Scherrer Institut, 5232 Villigen PSI, Switzerland

Received: December 20, 2008; Revised Manuscript Received: April 2, 2009

Phosphorus K-edge X-ray absorption fine structure (XAFS) was explored as a means to distinguish between aqueous and solid phosphates and to detect changes in phosphate protonation state. Data were collected for  $\text{H}_3\text{PO}_4$ ,  $\text{KH}_2\text{PO}_4$ ,  $\text{K}_2\text{HPO}_4$  and  $\text{K}_3\text{PO}_4$  solids and solutions and for the more complex phosphates, hydroxylapatite (HAP) and struvite (MAP). The X-ray absorption near-edge structure (XANES) spectra for solid samples are distinguishable from those of solutions by a shoulder at  $\sim 4.5$  eV above the edge, caused by scattering from cation sites. For phosphate species, the intensity of the white line peak increased for solid and decreased for aqueous samples, respectively, with phosphate deprotonation. This was assigned to increasing charge delocalization in solid samples, and the effect of solvating water molecules on charge for aqueous samples. In the extended X-ray absorption fine structure (EXAFS), backscattering from first-shell O atoms dominated the  $\chi(k)$  spectra. Multiple scattering (MS) via a four-legged  $\text{P}-\text{O}_1-\text{P}-\text{O}_1-\text{P}$  collinear path was localized in the lower  $k$  region at  $\sim 3.5 \text{ \AA}^{-1}$  and contributed significantly to the beat pattern of the first oscillation. For EXAFS analysis, increasing Debye–Waller factors suggest more disorder in the  $\text{P}-\text{O}$  shell with addition of protons to the crystal structure due to the lengthening effects of  $\text{P}-\text{OH}$  bonds. This disorder produces splitting in the hybridized  $\text{P } 3p-\text{O } 2p$  band in the density of states. For aqueous samples, however, increased protonation reduced the structural disorder within this shell. This was linked to a change from kosmotropic to chaotropic behavior of the phosphate species, with reduced effects of H bonding on structural distortion. The intensity of MS is correlated to the degree of disorder in the  $\text{P}-\text{O}$  shell, with more ordered structures exhibiting enhanced MS. The observed trends in the XAFS data can be used to distinguish between phosphate species in both solid and aqueous samples. This is applicable to many chemical, geochemical and biological systems, and may be an important tool for determining the behavior of phosphate during the hydrothermal gasification of biomass.

## 1. Introduction

The use of biomass as an alternate fuel source is of great interest as a means of alleviating dependence on nonrenewable energy resources and mitigating global warming. Production of synthetic natural gas (SNG) from biomass by hydrothermal gasification ( $T \geq 374 \text{ }^\circ\text{C}$ ;  $p \geq 22.1 \text{ MPa}$ ) has several advantages over conventional gasification procedures.<sup>1</sup> One such advantage is the potential for extraction and recovery of naturally occurring inorganic components, e.g., Ca, K, Mg, Na, P, S, N, from liquefied biomass stock during processing. As the solubility of dissolved inorganics decreases under hydrothermal conditions,<sup>2</sup> salts bearing the essential nutrients N, P, and K are precipitated and can be removed in a salt-separation step. This facilitates the recovery of inorganic material that can be recycled for use as fertilizer. In addition to simpler salts such as potassium phosphates, more complex salts such as hydroxylapatite (HAP) and struvite (magnesium ammonium phosphate hexahydrate, MAP) are likely precipitates. Both HAP and MAP occur naturally in geological and biological systems and importantly have been identified as a viable means of recovery of P from biomass sources such as sludge and wastewaters.<sup>3,4</sup>

To monitor precipitation during hydrothermal gasification, a technique is required that can distinguish between aqueous and

solid-phase phosphate. Changes in phosphate speciation in solution is also of interest as the ion product of water,  $K_w$  and thus pH, change under hydrothermal conditions.<sup>2</sup> Phosphate speciation including structure and hydration of species in solution has been explored using techniques such as infrared (IR) and Raman spectroscopy<sup>5,6</sup> and neutron scattering.<sup>7</sup> Various theoretical approaches have also been applied to calculate the structures of phosphate species in solution.<sup>8–11</sup> Previous work using P X-ray absorption fine structure (XAFS) has focused primarily on interpretation of X-ray absorption near-edge (XANES) spectra<sup>12–15</sup> or extended X-ray absorption spectroscopy (EXAFS) in solid P samples.<sup>16,17</sup> There is limited literature available on P EXAFS of aqueous samples,<sup>16</sup> likely due to the inherent complications of measurements requiring low-energy X-rays. This study uniquely combines P XANES and EXAFS to detect changes in phosphate speciation in both aqueous and solid samples. To the best of our knowledge, no previous study has used EXAFS as a technique to distinguish between phosphate protonation states in solution.

The utility of the XAFS technique in detecting changes in P speciation and the formation of P-bearing salts in systems at ambient  $T$  and  $p$  was explored. Though ultimately studies at higher conditions of  $T$  and  $p$  are necessary to understand P speciation under hydrothermal conditions, the first step was to determine the potential for use of XAFS under the simplest experimental conditions. Data are collected for both aqueous

\* Corresponding author. E-mail: Ashaki.Rouff@qc.cuny.edu. Current address: School of Earth and Environmental Sciences, Queens College CUNY, 65-30 Kissena Blvd., Flushing, NY 11367.

**TABLE 1: Speciation Calculations and Measured pH Values for Studied Solutions<sup>a</sup>**

solution 0.1 M	pH	% species				
		H <sub>3</sub> PO <sub>4</sub> <sup>0</sup>	H <sub>2</sub> PO <sub>4</sub> <sup>-</sup>	HPO <sub>4</sub> <sup>2-</sup>	PO <sub>4</sub> <sup>3-</sup>	KHPO <sub>4</sub> <sup>-</sup>
H <sub>3</sub> PO <sub>4</sub>	1.7	75	25			
KH <sub>2</sub> PO <sub>4</sub>	4.5		99			
K <sub>2</sub> HPO <sub>4</sub>	9.1			79		20
K <sub>3</sub> PO <sub>4</sub>	13			2	97	1

<sup>a</sup> Species <1% are omitted.

and solid samples of the simple phosphates H<sub>3</sub>PO<sub>4</sub>, KH<sub>2</sub>PO<sub>4</sub>, K<sub>2</sub>HPO<sub>4</sub>, and K<sub>3</sub>PO<sub>4</sub>. Solid samples of HAP (Ca<sub>5</sub>(PO<sub>4</sub>)<sub>3</sub>OH) and MAP (MgNH<sub>4</sub>PO<sub>4</sub>·6H<sub>2</sub>O), as potential phosphate-bearing products of the hydrothermal gasification salt-separation process, are also analyzed.

## 2. Experimental Section

**2.1. Sample Preparation.** Solutions were prepared from 85% H<sub>3</sub>PO<sub>4</sub>(aq), KH<sub>2</sub>PO<sub>4</sub>(s), K<sub>2</sub>HPO<sub>4</sub>(s) and K<sub>3</sub>PO<sub>4</sub>(s) in deionized water to generate 0.1 M solutions ranging from pH 1.5 to 13. Sample conditions including pH and calculated phosphate speciation are shown in Table 1. Aqueous speciation was calculated on the basis of the measured pH using the PHREEQC program with the llnl.dat database.<sup>18</sup> This confirmed that the phosphate species in the acid or solid used for solution preparation also dominated the aqueous-phase speciation, and solutions are subsequently referred to by this species. Solutions were mounted in ~100 μL Teflon liquid holders with 7.5 μm Kapton windows fixed with O rings and screws, for fluorescence measurements.

The three potassium phosphate solids along with HAP and MAP were selected for analysis. Finely ground solids were smeared on carbon tape and mounted on Cu plate holders for data collection in both fluorescence and total electron yield (TEY) mode.

**2.2. XAFS Data Collection and Analysis.** X-ray absorption fine structure (XAFS) spectra were collected at the LUCIA beamline (X07MA) at the Swiss Light Source (SLS), Villigen-PSI, Switzerland. The beamline was equipped with a Si(111) monochromator tuned to the P K-edge, assigned to 2145 eV using a white phosphorus (P) standard. Taking advantage of the small size of the X-ray spot (10 × 10 μm in our case), the stable beam position, and the high photon density, very demanding experiments in terms of sample environments can be performed.<sup>19</sup> This allowed for the introduction of a well-designed wet cell for the study of elements with low-energy absorption edges in solution. The cell must be transparent to low-energy X-rays, yet able to withstand the vacuum conditions required for these measurements. A Teflon holder with thin 7.5 μm Kapton windows was found to be suitable choice. The holder was placed in an experimental chamber under vacuum at ~10<sup>-3</sup>–10<sup>-4</sup> mbar and oriented at 45° to the incoming beam. The fluorescence yield was measured using an energy dispersive silicon drift diode (SDD) oriented at 90° to the sample and placed at a distance of 0.5 cm from the sample holder. For solids, the Cu sample holder was placed in the experimental chamber and oriented for data collection in fluorescence mode. The sample drain current as total electron yield (TEY) was also measured for solid samples. All measurements were conducted at ambient temperature.

Data reduction and fitting were performed with the WinXAS software package<sup>20</sup> using standard fitting procedures.<sup>21</sup> Theoretical backscattering phases and amplitudes and local density of

states were calculated with the FEFF 8<sup>22</sup> code using input files generated from crystal structure data of the studied solids.<sup>23–28</sup> The amplitude reduction factor,  $S_0^2$  was determined from first-shell fits to solid reference samples. Obtained values were averaged and  $S_0^2$  fixed at 0.8 for subsequent fits. Refinement was attempted in both  $k$  and  $R$  space using  $k^1$  weighted  $\chi$  functions  $\chi(k)$  and Fourier transforms  $FT(\chi(k))$ . For solutions,  $k$  space refinement was also done in  $k^2$  space, which amplified higher  $k$  oscillations in these spectra. For solid samples,  $k^2$  weighting significantly increased the noise in the high- $k$  region of the spectra and was therefore not applied. Structural parameters (degeneracy ( $N$ ), distance ( $R$ ), and Debye–Waller factor  $\sigma^2$ ) for each shell around the central P atom were assessed. For all samples, the degeneracy of the first O shell was fixed at 4, consistent with the coordination environment of the phosphate anion. Fits to second neighbor K shells were attempted for solid samples, but due to the limited  $k$  range of the  $\chi$  data, this yielded inconclusive results.

For multiple scattering (MS) within the PO<sub>4</sub> tetrahedron, the three-legged P–O<sub>1</sub>–O<sub>2</sub>–P triangular, four-legged P–O<sub>1</sub>–P–O<sub>2</sub>–P noncollinear and four-legged P–O<sub>1</sub>–P–O<sub>1</sub>–P collinear paths were assessed. Only the latter  $n$ -leg = 4 collinear MS path was found to be significant for PO<sub>4</sub>, consistent with observations by Rose et al.<sup>16</sup> for Fe–PO<sub>4</sub> systems. Several different models were attempted to fit the MS path, including correlating  $\sigma^2$  MS to 4 times that of the single scattering (SS) path, as is often applied to analogous AsO<sub>4</sub> tetrahedra.<sup>29</sup> However, a direct correlation between  $\sigma^2$  MS and that of the SS path, as implemented by Rose et al.,<sup>16</sup> was found to be the model most suited to fit MS in the PO<sub>4</sub> tetrahedron.

## 3. Results and Discussion

**3.1. XANES.** The XANES spectra for all samples are shown in Figure 1a. The near-edge spectra for all aqueous samples are quite similar and are easily distinguishable from those of the solid samples, which are more structured in the near-edge region. The edge energies, as determined from the second derivative of the absorption spectrum, along with peak and shoulder energies for all samples are listed in Table 2. Sample edge energies for all samples range from ~2151 to 2152 eV and are characteristic of the phosphate group.<sup>30</sup> The absorption at the edge is attributed to the transition of a 1s core electron to the 3p lowest unoccupied antibonding molecular orbital.<sup>12,13,31,32</sup> For all samples, the energy position of the white line peak (A) ranges from 2152–2153 eV. In addition, solid K-PO<sub>4</sub> samples display a visible shoulder (B) at ~4–5 eV above the edge with energy KH<sub>2</sub>PO<sub>4</sub> > K<sub>2</sub>HPO<sub>4</sub> ≈ K<sub>3</sub>PO<sub>4</sub>. This shoulder is also visible for the HAP sample spectrum, but not for the MAP sample spectrum. For Na, K, and Ca phosphates, this feature has been attributed to a second transition to a higher molecular orbital,<sup>33</sup> shape resonances<sup>12</sup> or multiple scattering effects.<sup>13</sup>

For XANES spectra of solid K–PO<sub>4</sub> samples, the white line is less intense and broader relative to the equivalent aqueous sample of each phosphate species. This is potentially due to more extensive bonding of phosphate in the solid phase relative to aqueous-phase phosphate species. In addition, the intensity of the white line appears to change with protonation. For solid samples, the intensity increases (Figure 1b), whereas for aqueous samples the intensity decreases (Figure 1c) with removal of protons. This trend in white line intensity may be due to differences in electronegativity between O and OH ligands, as well as the degree of charge delocalization for the relevant phosphate species.

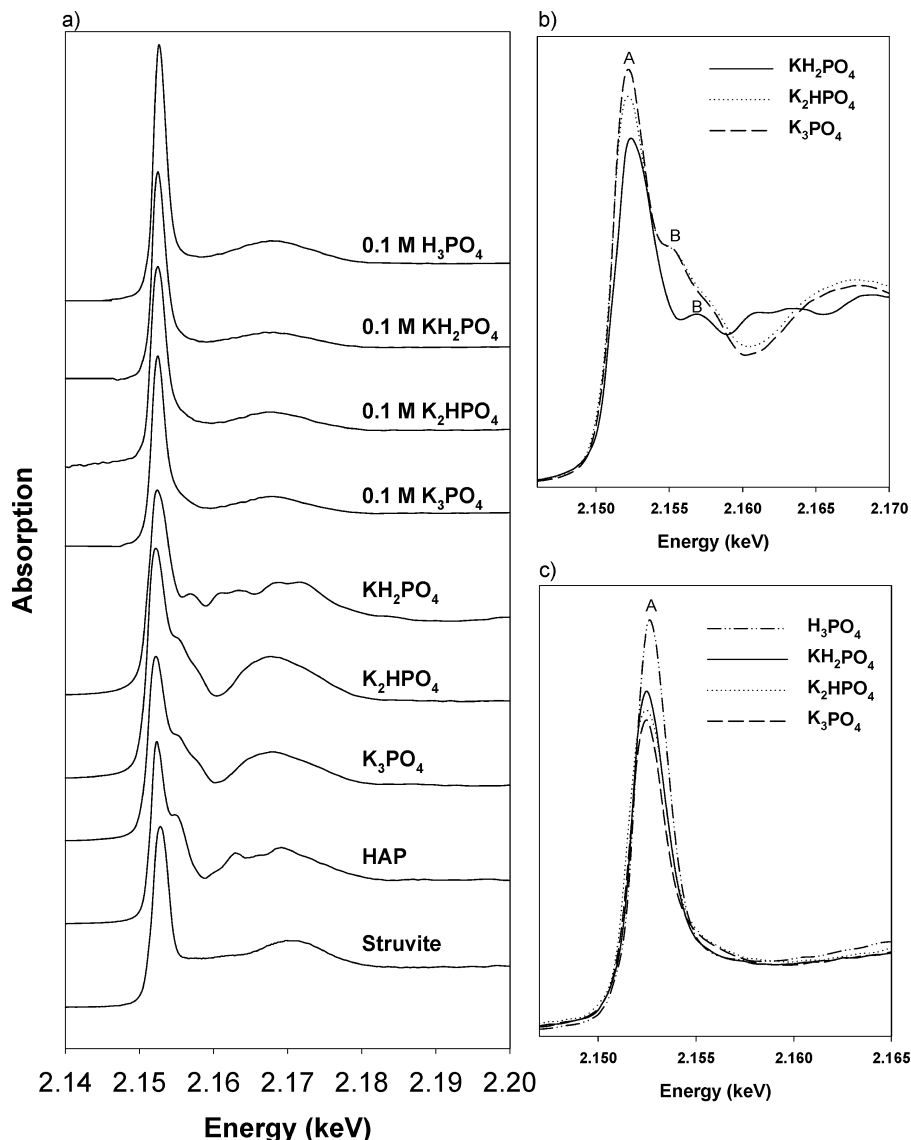


**Figure 1.** (a) XANES spectra for aqueous and solid samples. White line intensity (A) and comparison of structural features, including shoulder (B) for (b) solid and (c) aqueous samples.

**TABLE 2: Edge Energy, Energy Position of the White Line Peak (A) and Shoulder Energy (B) for Studied Samples**

solutions	edge (eV)	peak A (eV)	solids	edge (eV)	peak A (eV)	shoulder B (eV)
0.1 M $\text{H}_3\text{PO}_4$	2151.8	2152.6	$\text{KH}_2\text{PO}_4$	2151.2	2152.6	2156.8
0.1 M $\text{KH}_2\text{PO}_4$	2151.6	2152.6	$\text{K}_2\text{HPO}_4$	2151.1	2152.3	2155.0
0.1 M $\text{K}_2\text{HPO}_4$	2151.4	2152.5	$\text{K}_3\text{PO}_4$	2151.1	2152.3	2155.0
0.1 M $\text{K}_3\text{PO}_4$	2151.5	2152.5	HAP	2151.7	2152.4	2154.5
			MAP	2151.9	2152.8	

For solid samples, bonding to the more electronegative O ligands and complete delocalization of charge in the  $\text{PO}_4^{3-}$  species may result in the higher intensity peak relative to protonated species in which less electronegative OH ligands substitute and the charge becomes increasingly localized. The trend in white line intensity can also be inferred from density of states (DOS) calculations for the crystal structures. The DOS as calculated using FEFF 8<sup>22</sup> are shown in Figure 2. For all structures, several hybrid bands between s and p orbitals of P and O are evident in the  $-30$  to  $-15$  eV range, consistent with those observed for  $\text{PO}_4^{3-}$  in Ca, Mg, and Zn phosphates.<sup>34</sup> The band centered at about  $-17$  eV displays significant admixing between P 3p- and O 2p-like states, representing bonding between O and P. As protons are removed from the crystal structure, there is better overlap of P and O p-DOS in this region,

and peaks narrow and increase in intensity. This is likely to be reflected in the XANES, whereby an increasingly narrow density distribution and significant overlap between O and P orbitals might in turn increase the probability of electron transition, and thus the intensity of the white line peak.

For aqueous samples, the white line intensity is highest for  $\text{H}_3\text{PO}_4$ , suggesting that other factors, specifically the interaction with water via van der Waals forces or hydrogen bonding, may influence the charge distribution. Spectra for aqueous phosphate samples reported by Khare et al.<sup>15</sup> show increasing white line intensity  $\text{PO}_4^{3-} > \text{H}_3\text{PO}_4^0 > \text{H}_2\text{PO}_4^- > \text{HPO}_4^{2-}$ . The series is consistent with current observations with the exception of the  $\text{PO}_4^{3-}$  sample spectrum, which has the lowest white line intensity in our system, keeping with the protonation trend. The current solutions were prepared by simply dissolving the relevant

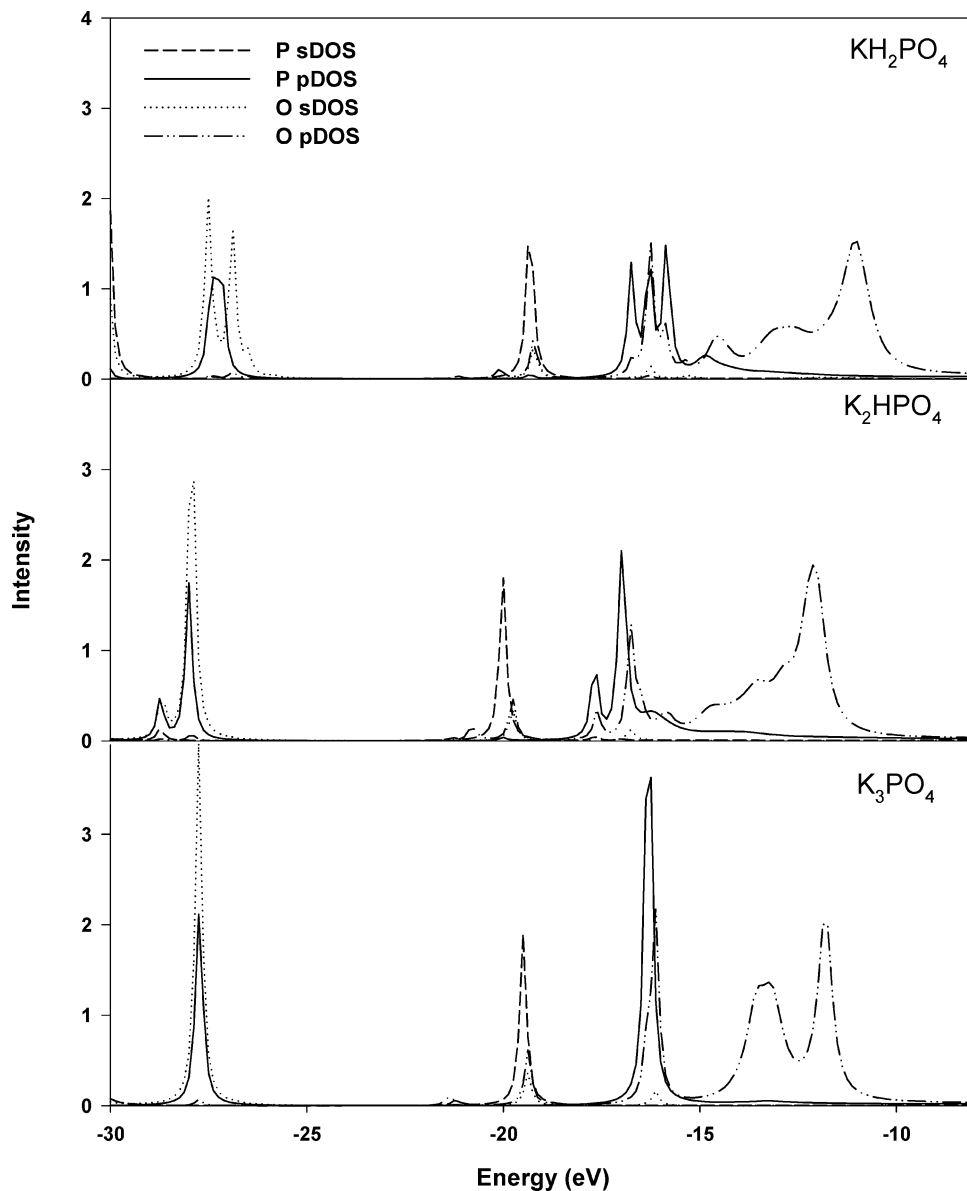


**Figure 2.** Total density of states (DOS) as calculated by FEFF 8 based on crystal structure data for solid samples. The energy axis refers to the FEFF calculated continuum level.

K salt and measuring the pH. The Khare et al.<sup>15</sup> samples may have been prepared from titration of phosphoric acid in perchlorate solutions. Thus the observed discrepancy may be due to differences in sample preparation and composition, pH, and potentially speciation. This, however, cannot be ascertained due to lack of information with respect to preparation of the Khare et al.<sup>15</sup> samples.

**3.2. EXAFS.** The experimental  $k^1$  weighted  $\chi(k)$  spectra and fits to the data for all samples are shown in Figure 3. The contributions of the O and MS paths to the fits are also displayed. For all samples, first-shell O atoms dominate the spectrum. The significant contribution from O backscattering is likely due to the strong covalent P–O bonding in the PO<sub>4</sub> tetrahedron. For all samples, a contribution to the  $\chi$  from the MS path is evident. The MS contribution is localized in the first oscillation, centered at  $\sim 3.5 \text{ \AA}^{-1}$ , significantly influencing the beat pattern in this region of the spectrum. This has also been observed for studies of AsO<sub>4</sub> sorption on Al and Fe oxides and clays, whereby inclusion of MS paths were required to reproduce the features in the first oscillation<sup>35</sup> and to improve the overall quality of fits to the data.<sup>29</sup>

The Fourier transformed  $\chi$  spectra are displayed in Figure 4a. In all cases the dominant peak centered at about 1.1–1.2 Å (uncorrected for phase shift) is associated with first-shell O atoms in tetrahedral coordination in the PO<sub>4</sub> structure. As observed in the near-edge region, the intensity of this peak varies with protonation. Peak intensity increases and decreases for solid (Figure 4b) and aqueous (Figure 4c) samples, respectively, with removal of protons from the phosphate structure. A trend similar to that of the solid samples has been observed for aqueous selenite samples with peak intensity  $\text{SeO}_3^{2-} > \text{HSeO}_3^- > \text{H}_2\text{SeO}_3$ .<sup>36</sup> This trend was attributed to increased formation of Se–OH single bonds and thus localization of the Se=O double bond with protonation. In the completely deprotonated selenite species, charge is delocalized and Se–O bonds are equivalent. Similarly, for solid phosphate samples, as discussed in the previous section, increased localization of the double bond with protonation, may result in the observed trend.

For all samples, a second peak can be observed in the 2.3–2.7 Å range (uncorrected for phase shift). This is unlikely to correspond to a K or second O shell, as for solid samples K neighbors are located at distances  $\geq 3.2 \text{ \AA}$ ,<sup>23,26,28</sup> whereas for



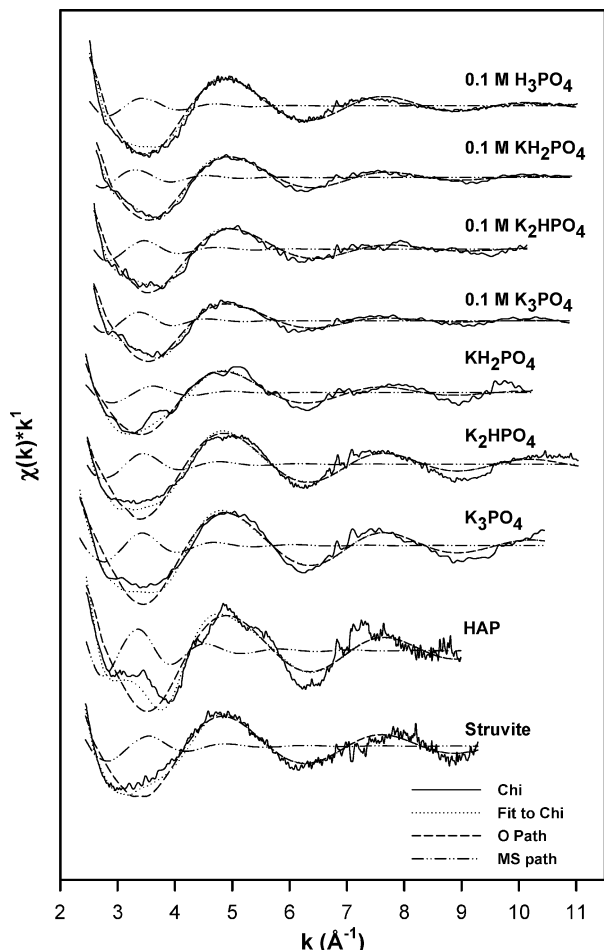


**Figure 3.** Experimental  $\chi$  data for all samples, showing fits to  $\chi$  and contributions of O and MS paths to fit.

aqueous samples O water molecules are likely to reside at distances  $\geq 3.7$  Å.<sup>7</sup> For protonated samples, crystal structure data indicate H neighbors in the 2.2–2.5 Å region. However, the peak is also observed for nonprotonated samples, in addition to which protons are unlikely to scatter X-rays. We therefore assign this peak to multiple scattering associated with first-shell O atoms in the phosphate tetrahedron. The position of this peak is consistent with findings of Rose et al.<sup>16</sup> for the  $n$ -leg = 4 collinear MS path.

**3.2.1. Effect of Protonation on the P–O shell.** EXAFS analysis results are displayed in Table 3. Though fitting was done in both  $k$  and  $R$  space, only results from  $R$  space fits are reported due to similarities in the obtained results. For K-PO<sub>4</sub> samples, the P–O distances in the PO<sub>4</sub> tetrahedron are 1.55 and 1.53–1.54 Å, for aqueous and solid samples, respectively. The P–O distance for aqueous samples is close to the free ion bond distance of 1.56 Å for PO<sub>4</sub>,<sup>37</sup> while that of solid samples is consistent with average P–O distances based on crystal structure data as reported in the literature.<sup>23,26–28</sup> This alludes to some relaxation of the structure in solution. However, as the range of observed P–O distances for all samples falls within the 0.02 Å uncertainty for first-shell distances, this cannot be ascertained.

First shell Debye–Waller factors ( $\sigma^2$ ) show noticeable trends. For each of the K–PO<sub>4</sub> samples, the  $\sigma^2$  value for the aqueous sample is higher than that of the solid sample, suggestive of a higher degree of thermal and structural disorder in the aqueous phase. The  $\sigma^2$  value also varies with protonation. For solid samples,  $\sigma^2$  decreases, whereas for aqueous samples,  $\sigma^2$  increases

with deprotonation. For solid samples, the trend in  $\sigma^2$  implies that removal of protons from the crystal structure results in a decrease in bond length distribution in the PO<sub>4</sub> tetrahedron. This is consistent with structural data, which indicates significant elongation of the P–OH relative to the P–O bond in the crystal structure, and thus a wider distribution about the average bond length for these samples. However, for the equivalent aqueous samples, the opposite trend is observed. For PO<sub>4</sub> in solution, with increasing basicity and loss of protons, the structure of the species in solution becomes more disordered, as indicated by  $\sigma^2$  for H<sub>3</sub>PO<sub>4</sub><sup>0</sup> < H<sub>2</sub>PO<sub>4</sub><sup>2−</sup> < HPO<sub>4</sub><sup>2−</sup> < PO<sub>4</sub><sup>3−</sup>.

For solids, bonding between P–O is indicated by the overlap of P 3p and O 2p orbitals in the DOS plot (Figure 2). Splitting of this band, centered at about −17 eV, is evident for KH<sub>2</sub>PO<sub>4</sub> and K<sub>2</sub>HPO<sub>4</sub> structures and may be linked to the distortion of the phosphate tetrahedron with addition of protons. A correlation between electronic properties and geometrical changes was previously observed for Ca<sub>3</sub>(PO<sub>4</sub>)<sub>2</sub>–Zn<sub>3</sub>(PO<sub>4</sub>)<sub>2</sub> solid solutions.<sup>34</sup> Substitution of Zn into the Ca<sub>3</sub>(PO<sub>4</sub>)<sub>2</sub> structure resulted in pronounced splitting of peaks in the DOS, equivalent to those centered at −17 eV in the current study. This was attributed to increased distortion of the structure due to the spread in Zn–O bond lengths for the Zn<sub>3</sub>(PO<sub>4</sub>)<sub>2</sub> end member.<sup>34</sup> For the relatively undistorted PO<sub>4</sub> tetrahedron in K<sub>3</sub>PO<sub>4</sub>, a well-defined narrow peak is observed at approximately −17 eV. However, for protonated samples, peak splitting follows the trend K<sub>2</sub>HPO<sub>4</sub> < KH<sub>2</sub>PO<sub>4</sub>. This is consistent with increased bond length distribution due to protonation, and thus increased disorder in the P–O shell, as indicated by the trend in Debye–Waller factors.

For PO<sub>4</sub> in solution, PO<sub>4</sub><sup>3−</sup> and HPO<sub>4</sub><sup>2−</sup> are characterized as “structure makers” or kosmotropes, whereas H<sub>2</sub>PO<sub>4</sub><sup>−</sup> is a structure breaker or chaotrope.<sup>11</sup> This means that PO<sub>4</sub><sup>3−</sup>–H<sub>2</sub>O bonds are stronger than H<sub>2</sub>O–H<sub>2</sub>O bonds, whereas H<sub>2</sub>PO<sub>4</sub><sup>−</sup>–H<sub>2</sub>O bonds are weaker than H<sub>2</sub>O–H<sub>2</sub>O bonds. For the series PO<sub>4</sub><sup>3−</sup>, HPO<sub>4</sub><sup>2−</sup>, H<sub>2</sub>PO<sub>4</sub><sup>−</sup> and H<sub>3</sub>PO<sub>4</sub>, the charge on each O atom is −0.75, −0.5, −0.25, and 0, and P–O units interact more strongly with water relative to P–OH units.<sup>7</sup> Therefore PO<sub>4</sub><sup>3−</sup> forms the strongest H bonds to water with a well-defined hydration sphere with  $\sim 15 \pm 3$  water molecules.<sup>7</sup> This means that water molecules interact strongly with PO<sub>4</sub><sup>3−</sup> in solution and these strong interactions are more likely to distort the PO<sub>4</sub><sup>3−</sup> tetrahedron, relative to the increasingly weaker, less structured hydration spheres of the protonated anions. In addition, more H bonds in water are broken in the presence of kosmotropes, suggesting that the structure of H<sub>2</sub>O around the PO<sub>4</sub><sup>3−</sup> anion is somewhat disrupted.<sup>11</sup> Enhanced H-bond breakage in the vicinity of the anion may in turn result in further distortion of P–O bond lengths in the tetrahedron. Thus as the anion loses protons and H bonding increasingly proceeds via P–O bonds, the overall interaction of the anion with water molecules becomes stronger, resulting in a greater propensity for distortion of the phosphate tetrahedron.

**3.2.2. Multiple Scattering.** The  $n$ -leg = 4 collinear MS path for all samples was fit by correlating  $\sigma^2$  MS to that of  $\sigma^2$  O (Table 3).

As the MS path is collinear, it can be inferred that scattering may be more sensitive to very small differences in the P–O bond lengths of more ordered tetrahedra. This may in turn reduce the overall amplitude for MS paths involving displaced O atoms. As protonated O atoms are more likely to be displaced, deprotonated O atoms may potentially be more susceptible to MS in the phosphate structure.

To explore the effect of P–O bond distribution on MS from individual O atoms in the PO<sub>4</sub> tetrahedron and the role

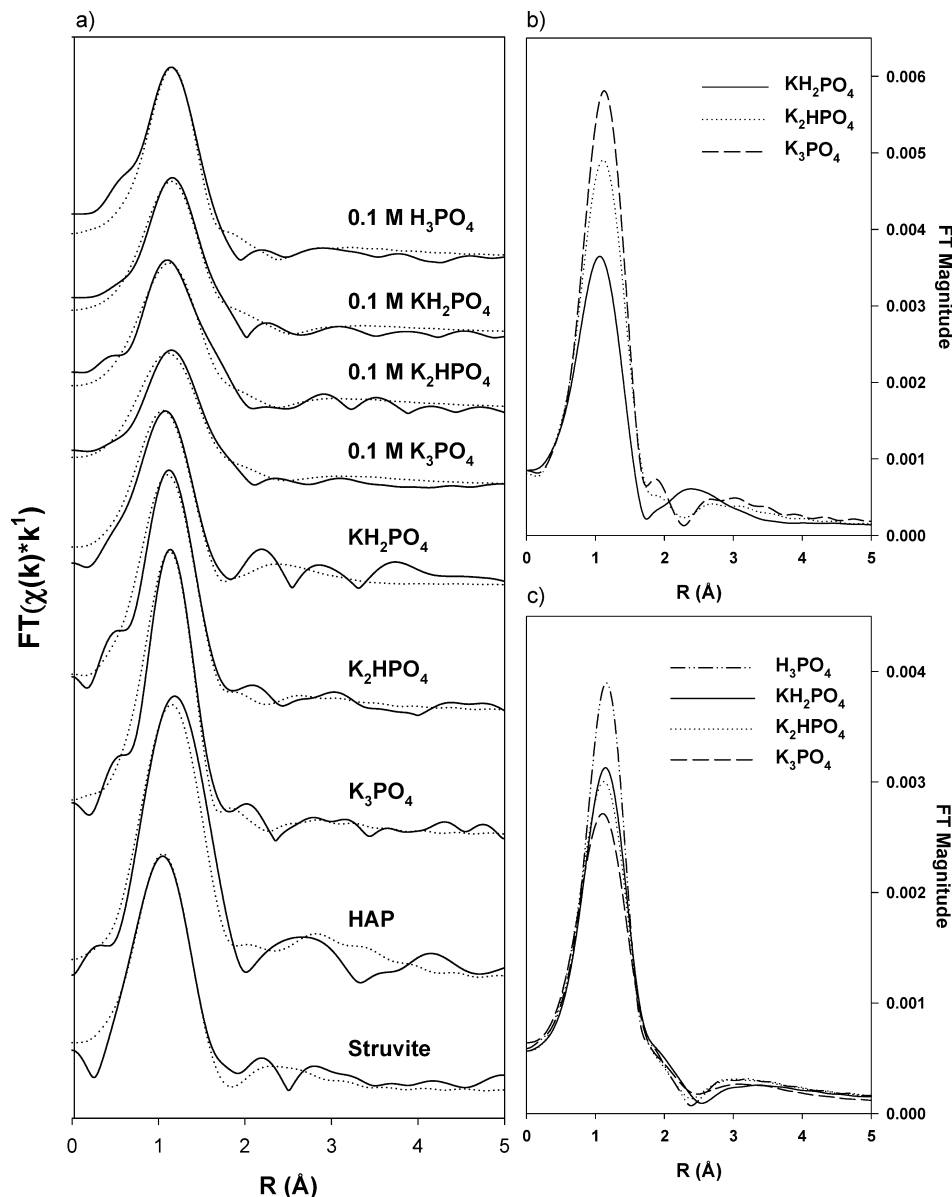


**Figure 4.** (a) Experimental Fourier transforms of chi spectra and fits to data for all samples. Comparison of Fourier transform magnitude for first shell O for (b) solid and (c) aqueous samples. Only fits to data are shown.

of protonation on MS, the theoretical paths, as calculated from crystal structure data<sup>23,26–28</sup> using the FEFF 8 code,<sup>22</sup> were examined. The P–O distances for each atom in the phosphate tetrahedron, as determined from structural data, are shown in Table 4. Protonated O atoms have P–O distances of 0.05–0.10 Å longer than those of deprotonated O atoms, and theoretical calculations indicate that the amplitude of the MS is indeed lower for protonated O atoms. However, the amplitude ratio is close to that of deprotonated O atoms with the exception of the  $KH_2PO_4$  structure. This may be due to the regularity in P–O bond length distribution for this structure, whereby the P–O distances of both O1 and O2, and both protonated O3 and O4 are equivalent. The effect of the two protons on the structure may in turn enhance the MS for the deprotonated O atoms at a distance closer to the P core.

For the  $K_3PO_4$  structure in which there are no protonated O atoms, O3 and O4 lie at a distance of 0.01–0.02 Å longer than that of O1 and O2. Though this difference is not as significant as that between protonated and deprotonated O atoms in the other structures, there is a notable amplitude

reduction for the MS path for these two latter O atoms. In this structure the distribution of P–O bond lengths is relatively uniform and charge is completely delocalized in the phosphate tetrahedron. Thus it appears that even small displacements in the P–O bond lengths significantly affect MS and enhance this phenomenon for the O atoms at shorter distances. In addition, the relative amplitudes of less significant P–O<sub>1</sub>–P–O<sub>2</sub> paths are also higher relative to other structures indicating overall increased sensitivity to MS in this structure.

These observations are directly related to the symmetry of the different phosphate species, whereby  $PO_4^{3-}$  has  $T_d$  (tetrahedral),  $H_2PO_4^{2-}$   $C_{2v}$  (cis-planar), and  $HPO_4^-$  and  $H_3PO_4$   $C_{3v}$  (trigonal pyramidal) symmetry. For protonated species, MS is likely to be more effective in the higher symmetry  $H_2PO_4^{2-}$  planar complex relative to the lower symmetry trigonal pyramidal complexes formed by  $HPO_4^-$  and  $H_3PO_4$  species. In turn, MS is likely to be most important in the high-symmetry tetrahedral  $PO_4^{3-}$  complex compared to protonated phosphate species, giving rise to higher order multiple-scattering effects. As the overall symmetry of these

**TABLE 3: Structural Parameters Derived from Best Fits in *R*-Space to the First Shell O Atoms and the *n*-leg = 4, Collinear Multiple Scattering Shell**

	sample	shell	<i>N</i> <sup>a</sup>	<i>R</i> <sup>b</sup> (Å)	$\sigma^2$ <sup>c</sup> (Å <sup>2</sup> )	$\Delta E_0$ <sup>d</sup> (eV)	$\chi^2$ <sup>e</sup>	% res <sup>f</sup>
solutions	0.1 M H <sub>3</sub> PO <sub>4</sub>	O	4	1.55	0.005	7.5	47	10
		MS	2.8	3.21	0.005	7.5		
	0.1 M KH <sub>2</sub> PO <sub>4</sub>	O	4	1.55	0.009	7.7	23	11
		MS	3.0	3.25	0.009	7.7		
	0.1 M K <sub>2</sub> HPO <sub>4</sub>	O	4	1.55	0.010	7.0	30	13
		MS	3.4	3.20	0.010	7.0		
	0.1 M K <sub>3</sub> PO <sub>4</sub>	O	4	1.55	0.013	5.3	100	14
		MS	3.2	3.23	0.013	5.3		
solids	KH <sub>2</sub> PO <sub>4</sub>	O	4	1.53	0.007	1.9	44	15
		MS	3.3	2.94	0.007	1.9		
	K <sub>2</sub> HPO <sub>4</sub>	O	4	1.54	0.003	3.7	191	15
		MS	2.9	3.16	0.003	3.7		
	K <sub>3</sub> PO <sub>4</sub>	O	4	1.54	0.002	3.3	270	13
		MS	2.2	3.18	0.002	3.3		
	HAP	O	4	1.52	0.002	5.1	186	11
		MS	4.5	3.20	0.002	5.1		
	MAP	O	4	1.52	0.002	0.2	135	11
		MS	3.8	3.00	0.002	0.2		

<sup>a</sup> Degeneracy. <sup>b</sup> Distance. <sup>c</sup> Debye–Waller. <sup>d</sup> Energy shift. <sup>e</sup> Reduced  $\chi^2$  or goodness of fit. <sup>f</sup> % Residual. First shell errors: *N* = 20%; *R* = 0.02 Å;  $\sigma^2$  = 0.002 Å<sup>2</sup>.

**TABLE 4: Phosphate Tetrahedron O Distances from Structural Data and Amplitude Ratios for MS Paths from Theoretical Calculations**

structure	distance (Å)				amplitude ratio for MS path <sup>b</sup>			
	O1	O2	O3	O4	O1	O2	O3	O4
H <sub>3</sub> PO <sub>4</sub>	1.50	1.55 <sup>a</sup>	1.55 <sup>a</sup>	1.55 <sup>a</sup>	1	0.9 <sup>a</sup>	0.9 <sup>a</sup>	0.8 <sup>a</sup>
KH <sub>2</sub> PO <sub>4</sub>	1.50	1.50	1.57 <sup>a</sup>	1.57 <sup>a</sup>	1	1	0.4 <sup>a</sup>	0.4 <sup>a</sup>
K <sub>2</sub> HPO <sub>4</sub>	1.51	1.51	1.52	1.61 <sup>a</sup>	1	1	1	0.7 <sup>a</sup>
K <sub>3</sub> PO <sub>4</sub>	1.52	1.52	1.53	1.54	1	1	0.5	0.5

<sup>a</sup> Protonated O atoms <sup>b</sup> Amplitude relative to O1.

complexes varies significantly with the number and addition of solvating water molecules to the structure, this rationale is most applicable to solid-phase samples.

Overall, it appears that the symmetry, and thus the uniformity of the phosphate structure, rather than solely the protonation state, influences the MS phenomenon. A more uniform, symmetrical structure is more sensitive to slight differences in bond lengths. This results in a significant reduction in MS for displaced O atoms, relative to those at shorter P–O distances. In the case of the KH<sub>2</sub>PO<sub>4</sub> structure, displacement of O atoms is due to protonation, whereas for the K<sub>3</sub>PO<sub>4</sub> structure these atoms are deprotonated. In addition, the overall amplitude of the O1 MS path decreases in the order K<sub>3</sub>PO<sub>4</sub> > K<sub>2</sub>HPO<sub>4</sub> ≈ KH<sub>2</sub>PO<sub>4</sub> > H<sub>3</sub>PO<sub>4</sub>, emphasizing the enhanced propensity for multiple scattering in the relatively undistorted, high-symmetry PO<sub>4</sub><sup>3−</sup> tetrahedron in the solid phase. In the aqueous phase, as discussed above, the PO<sub>4</sub><sup>3−</sup> species is more susceptible to the influence of solvating water molecules relative to protonated species, which in turn is likely to affect the MS properties of the structure.

**3.3. More Complex Phosphates.** XAFS data were also collected for hydroxylapatite and struvite solids for comparison with simpler K phosphate salts. The XANES spectra for both HAP and MAP are consistent with those previously reported in the literature.<sup>14,38,39</sup> The XANES spectrum for HAP is similar to that of the K-salts, whereby two distinct peaks (A and B) are noted in the spectrum. In the case of MAP, the second peak or shoulder (B) is not evident in the XANES spectrum. The presence of this shoulder has been

**TABLE 5: Coordination Numbers and Average Distances for Cation Sites in Solid Samples As Determined from Crystal Structure Data<sup>23–28</sup>**

Structure	shell	CN	<i>R</i> (Å)	std dev (Å)
KH <sub>2</sub> PO <sub>4</sub>	P–K	6	3.64	0.13
K <sub>2</sub> HPO <sub>4</sub>	P–K	6	3.44	0.12
K <sub>3</sub> PO <sub>4</sub>	P–K	7	3.36	0.12
HAP	P–Ca	9	3.42	0.22
Struvite	P–N	1	3.77	
	P–Mg	3	4.53	0.23

attributed to continuum resonances that reflect chemical changes beyond the first shell, specifically MS processes involving cation sites.<sup>12</sup> Thus, the distance of these cation sites from the core may be important in determining the intensity of feature B. Based on crystal structure data, the second shell P–K distance for K–PO<sub>4</sub> salts ranges from 3.36–3.64 Å and the average Ca–P distance in HAP is 3.42 Å (Table 5). The P–N and P–Mg distances in struvite at 3.77 and 4.53 Å, respectively, are longer compared to the interatomic distances in both K–PO<sub>4</sub> salts and HAP. In addition, the number of coordinating N and Mg atoms in these shells is low and both are weak backscatters relative to K and Ca. Thus, the longer distance between the P absorber and NH<sub>4</sub> and Mg sites, combined with low coordination numbers and weak backscattering from these shells is likely to reduce the effects of MS from these sites. As peak B is a product of this MS, its intensity is affected such that it is not evident in the MAP spectrum.

For the EXAFS data, the contribution of MS from first-shell O atoms to the first oscillation in the  $\chi$  spectrum of HAP is significantly enhanced relative to other phosphate samples. This is also reflected in fit results that are indicative of significant MS in this crystal structure. For MAP, the effect of MS appears to be more significant relative to simpler phosphates, but less so than in HAP. These results suggest that MS in the phosphate structure might be enhanced in more complex mineral phases, relative to simpler solids, such as the K–PO<sub>4</sub> solid series studied here. This may be due to the presence and complicating effects of a number of different ions in the matrix with which phosphate is likely to be interacting significantly. Based on combined XANES and

EXAFS data, HAP is easily distinguishable from MAP solid, both of which can be distinguished from simpler  $\text{K-PO}_4$  solid phases.

#### 4. Summary and Conclusion

The use of XAFS to distinguish between different solid and aqueous-phase phosphate species has been explored. For XANES data, the most notable difference between aqueous and solid spectra is a visible shoulder at  $\sim 4.5$  eV above the edge for solid samples due to MS from cation sites. The intensity of the white line peak increases for solid samples but decreases for aqueous samples with removal of protons from the structure. For solid samples, this is potentially due to the degree of charge delocalization, which is dependent on the number of P–O and P–OH bonds. The trend in white line intensity corresponds to trends in the DOS for these structures, with better P and O pDOS overlap with removal of protons from the solid structure. In the case of aqueous species, van der Waals interactions and hydrogen bonding with solvating water molecules is likely to influence the white line intensity. EXAFS fits to first shell O atoms indicate trends in Debye–Waller factors, which suggest that addition of protons to phosphate reduces the structural disorder of the resultant anion for aqueous samples, but increases that for solid samples. For aqueous samples, reduced interaction of P–OH relative to P–O bonds with solvating water molecules may contribute to a more ordered shell. For solid samples, significant bond length distribution with addition of protons to the structure is due to elongated P–OH relative to P–O bonds. This distortion produces splitting in the hybridized P 3p–O 2p band in the DOS.

For all samples, the lower region of the  $\chi(k)$  spectrum is dominated by multiple scattering within the phosphate structure. The most significant contribution to this phenomenon was found to be a 4-legged P–O<sub>1</sub>–P–O<sub>1</sub>–P collinear path. The multiple scattering phenomenon in K–phosphate solids and aqueous samples appears to be strongly influenced by the overall structural disorder in the phosphate tetrahedron of the species. The effect of protonation on MS is most evident for the  $\text{KH}_2\text{PO}_4$  solid, in which MS for deprotonated O atoms is enhanced relative to those of  $\text{H}_3\text{PO}_4$  and  $\text{K}_2\text{HPO}_4$  solids. This may be related to the higher order symmetry of  $\text{H}_2\text{PO}_4^-$  relative to  $\text{H}_3\text{PO}_4^0$  and  $\text{HPO}_4^{2-}$  structures. For  $\text{K}_3\text{PO}_4$ , the well-ordered high-symmetry  $T_d$  configuration of  $\text{PO}_4^{3-}$  means that small displacements in the P–O bond lengths may significantly affect MS, thus enhancing this phenomenon for the O atoms at shorter distances. Overall, solid and aqueous samples show distinct trends in Debye–Waller factors and multiple scattering with changing phosphate speciation.

In summary, XAFS is a viable technique for studying phosphate aqueous–solid transitions due to distinct differences in spectra for phosphate in these phases. Changes in speciation of the phosphate anion due to protonation in both aqueous and solid phases are, however, more subtle. Phosphate speciation in unknown samples can be estimated by comparison of relative trends in Debye–Waller factors and multiple scattering effects to that of well-characterized references in which the phosphate speciation is known. Though the ultimate goal of this study is to use ambient data to discern the potential use of XAFS for exploration of high- $T$  and - $p$  systems, these findings are applicable to phosphate EXAFS in other systems. These include the study of phosphate contaminated soils and other geochemical settings in which heavy metal sequestration by phosphate minerals

and phosphate ternary complexes may be of interest. In biological systems phosphate is an important component of tissue, DNA, and bones and is precipitated in biologically mediated processes, such as kidney stone formation. Thus the development of XAFS as a tool for probing the local structure of P in both the solid and aqueous phase is widely applicable beyond the main interests of this study.

**Acknowledgment.** This research was funded by the Swiss National Science Foundation, grant number 200021-109572. Thanks to Markus Janousch and Thomas Huthwelker of the LUCIA beamline (X07MA) and Erich De Boni, Peter Hottinger, Sebastian Sonderegger, and Charles Zumbach (PSI) for their support and contributions to this research. Comments from three anonymous reviewers significantly improved this manuscript.

#### References and Notes

- (1) Peterson, A. A.; Vogel, F.; Lachance, R. P.; Fröling, M.; Antal, M. J.; Tester, J. W. *Energy Environ. Sci.* **2008**, *1*, 32–65.
- (2) Hodes, M.; Marrone, P. A.; Hong, G. T.; Smith, K. A.; Tester, J. W. *J. Supercrit. Fluids* **2004**, *29*, 265–288.
- (3) Donnet, D.; Salecker, M. *Environ. Technol.* **1999**, *20*, 735–742.
- (4) Doyle, J. D.; Parsons, S. A. *Water Res.* **2002**, *36*, 3925–3940.
- (5) Preston, C. M.; Adams, W. A. *J. Phys. Chem.* **1979**, *83*, 814–821.
- (6) Rudolph, W. W.; Irmer, G. *Appl. Spectrosc.* **2007**, *61*, 1312–1327.
- (7) Mason, P. E.; Cruickshank, J. M.; Neilson, G. W.; Buchanan, P. *Phys. Chem. Chem. Phys.* **2003**, *5*, 4686–4690.
- (8) Pye, C. C.; Michels, M. R. *Can. J. Anal. Sci. Spectrosc.* **2004**, *49*, 175–184.
- (9) Pye, C. C.; Michels, M. R. *Can. J. Anal. Sci. Spectrosc.* **2005**, *50*, 70–86.
- (10) Ebner, C.; Onthong, U.; Probst, M. *J. Mol. Liq.* **2005**, *118*, 15–25.
- (11) Brandán, S. A.; Díaz, S. B.; Picot, R. C.; Disalvo, E. A.; Ben Altabef, A. *Spectrochim. Acta, Part A* **2007**, *66*, 1152–1164.
- (12) Franke, R.; Holmes, J. *Phys. B* **1995**, *216*, 85–95.
- (13) Sugiura, C.; Kamata, A.; Kashiwakura, T.; Tezuka, H.; Suzuki, K.; Nakai, S. *J. Phys. Soc. Jpn.* **1997**, *66*, 274–275.
- (14) Hesterberg, D.; Zhou, W.; Hutchinson, K. J.; Beauchemin, D.; Sayers, D. E. *J. Synchrotron Rad.* **1999**, *6*, 636–638.
- (15) Khare, N.; Martin, J. D.; Hesterberg, D. *Geochim. Cosmochim. Acta* **2007**, *71*, 4405–4415.
- (16) Rose, J.; Flank, A.; Mason, A.; Bottero, J.; Elmerich, P. *Langmuir* **1997**, *13*, 1827–1834.
- (17) Mondal, K.; Sthitsuksanoh, S. B.; Lalvani, S. B. *J. Mater. Sci. Lett.* **2003**, *22*, 95–97.
- (18) Parkhurst, D. L.; Appelo, C. A. J. *User's guide to PHREEQC (Version 2)–A computer program for speciation, batch-reaction, one-dimensional transport, and inverse geochemical calculations*; Water-Resources Investigations Report 99-4259; U.S. Geological Survey: Washington, DC, 1999, 310 pp.
- (19) Flank, A. M.; Cauchon, G.; Lagarde, P.; Bac, S.; Janousch, M.; Wetter, R.; Dubuisson, J.-M.; Idir, M.; Langlois, F.; Moreno, T.; Vantelon, D. *Nucl. Instrum. Methods Phys. Res., Sect. B* **2006**, *246*, 269–274.
- (20) Ressler, T. *J. Synchrotron Rad.* **1981**, *5*, 118–122.
- (21) Fendorf, S. E.; Sparks, D. L.; Lamble, G. M.; Kelley, M. J. *Soil Sci. Soc. Am. J.* **1994**, *58*, 1583–1595.
- (22) Zabinsky, S. I.; Rehr, J. J.; Ankudinov, A.; Albers, R. C.; Eller, M. J. *Phys. Rev. B* **1995**, *52*, 2995–3009.
- (23) Baur, W. H. *Acta Crystallogr., Sect. B* **1973**, *29*, 2726–2731.
- (24) Ferraris, G.; Fuess, H.; Joswig, W. *Acta Crystallogr., Sect. B* **1986**, *42*, 253–258.
- (25) Hughes, J. M.; Cameron, M.; Crowley, K. D. *Am. Mineral.* **1989**, *74*, 870–876.
- (26) Lis, T. *Acta Crystallogr., Sect. C* **1994**, *C50*, 484–487.
- (27) Moss, G. R.; Souhassou, M.; Espinosa, E.; Lecomte, C.; Blessing, R. H. *Acta Crystallogr., Sect. B* **1995**, *B51*, 650–660.
- (28) Voronin, V. I.; Ponomov, Yu. S.; Berger, I. F.; Proskurnina, N. V.; Zubkov, V. G.; Tyutyunnik, A. P.; Bushmeleva, S. N.; Balagurov, A. M.; Sheptyakov, D. V.; Burmakina, E. I.; Shekhtman, G. Sh.; Vovkotrub, E. G. *Inorg. Mater.* **2006**, *42*, 908–913.
- (29) Voegelin, A.; Weber, F.; Kretschmar, R. *Geochim. Cosmochim. Acta* **2007**, *71*, 5804–5820.
- (30) Cavell, R. G.; Barnes, E. M.; Arboleda, P. H.; Cavell, P. A.; Feng, F.; Gordon, R. A.; Webb, M. A. *Am. Mineral.* **2004**, *89*, 519–526.
- (31) Kuper, G. *Chem. Phys.* **1992**, *165*, 405–414.
- (32) Yin, Z. F.; Kasrai, M.; Bancroft, G. M.; Tan, K. H.; Feng, X. H. *Phys. Rev.* **1995**, *51*, 742–750.



- (33) Yoshii, K.; Baba, Y.; Sasaki, T. A. *J. Phys.: Condens. Matter* **1997**, 9, 2839–2847.
- (34) Yin, X.; Claderin, L.; Stott, M. J.; Sayer, M. *Biomaterials* **2002**, 23, 4155–4163.
- (35) Beaulieu, B. T.; Savage, K. S. *Environ. Sci. Technol.* **2005**, 39, 3571–3579.
- (36) Peak, D.; Saha, U. K.; Huang, P. M. *Soil Sci. Soc. Am. J.* **2006**, 70, 192–203.
- (37) Höjer, G.; Meza-Höjer, S.; Hernández de Pedrero, G. *Chem. Phys. Lett.* **1976**, 37, 301–306.
- (38) Siritapetawee, J.; Pattanasiriwisawa, W. *J. Synchrotron Rad.* **2008**, 15, 158–161.
- (39) Güngör, J.; Jürgensen, A.; Karthikeyan, K. J. *J. Environ. Qual.* **2007**, 36, 1856–1863.

JP811276T